Optics Letters

Mapping electron-beam-injected trapped charge with scattering scanning near-field optical microscopy

Denis E. Tranca,[1] Emilio Sánchez-Ortiga,[2] Genaro Saavedra,[2] Manuel Martínez-Corral,[2] Syed A. M. Tofail,[3] Stefan G. Stanciu,[1] Radu Hristu,[1] and George A. Stanciu[1,*]

[1]Center for Microscopy—Microanalysis and Information Processing, University Politehnica of Bucharest, Bucharest RO-060042, Romania
[2]3D Imaging and Display Laboratory, Department of Optics, University of Valencia, Valencia 46100, Spain
[3]Department of Physics and Energy, and Materials and Surface Science Institute, University of Limerick, Limerick, Ireland
*Corresponding author: stanciu@physics.pub.ro

Received 17 December 2015; accepted 11 January 2016; posted 19 January 2016 (Doc. ID 255969); published 1 March 2016

Scattering scanning near-field optical microscopy (s-SNOM) has been demonstrated as a valuable tool for mapping the optical and optoelectronic properties of materials with nanoscale resolution. Here we report experimental evidence that trapped electric charges injected by an electron beam at the surface of dielectric samples affect the sample–dipole interaction, which has direct impact on the s-SNOM image content. Nanoscale mapping of the surface trapped charge holds significant potential for the precise tailoring of the electrostatic properties of dielectric and semiconductive samples, such as hydroxyapatite, which has particular importance with respect to biomedical applications. The methodology developed here is highly relevant to semiconductor device fabrication as well.

OCIS codes: (180.4243) Near-field microscopy; (160.1435) Biomaterials; (090.1995) Digital holography; (120.6650) Surface measurements, figure.

http://dx.doi.org/10.1364/OL.41.001046

Scattering scanning near-field optical microscopy (s-SNOM) has been demonstrated in the past as an extremely effective tool for imaging and mapping the surface properties of materials in the nanoscale. The complex contrast mechanisms of s-SNOM have enabled a wide range of applications such as electric permittivity mapping [1,2], infrared spectroscopy measurements [3–5], and plasmonic response investigations [6,7] with resolution beyond the diffraction limit [8,9]. The functionality of this microscopy tool is based on local interactions between the tip of a nano-probe that is scanned across the sample surface and the molecules on the sample surface in the presence of an incident laser beam focused on the tip. The electric field component of the incident laser beam creates in the tip an oscillating electric dipole which emits light with the same wavelength as the incident beam [10,11]. When the tip is in close proximity to the surface of a sample (at distances much shorter than the wavelength), the light emitted by the electric dipole is influenced (in terms of amplitude and phase of the electric field component) by the local dielectric function of the sample. Detecting the light emitted by the oscillating electric dipole requires higher-harmonic demodulation and interferometric detection techniques to suppress the background light (mainly composed of direct or multiple reflections from the probe and sample) and to facilitate the reconstruction of the near-field optical signal amplitude and phase.

Our experiment brings evidence that trapped charges (e.g., injected by an electron beam or an ion beam, both of which are common in semiconductor device processing and biomaterials sterilization) influence the oscillating dipole from the tip and thus directly impact the image contrast in s-SNOM. We exploit this phenomenon to use s-SNOM imaging for mapping trapped surface charge with nanoscale resolution.

The interaction between trapped electrical charges and an oscillating dipole in s-SNOM can be understood by recalling that the latter models the oscillations of plasma electrons from the metal tip. In the first half-cycle of the external oscillating electric field [Fig. 1(a)], the field points to the tip from the sample. The plasma electrons in the tip are then directed toward the sample. In the case when no trapped charge is present on the surface, we assume that at the maximum elongation of the dipole an electric field of amplitude E_o is generated at the tip. Conversely, when a trapped charge is present at the surface in the proximity of the tip, a repulsive electric force occurs between the trapped charge and the plasma electrons at the tip–material surface interface. As a result, the elongation of the plasma electrons' oscillation decreases, which results in a decrease ΔE of the amplitude of the generated electric field. In the second half-cycle of the incident electric field [Fig. 1(b)], the field is pointing from the tip to the sample. In this case, the plasma electrons from the tip are directed backward from the sample. Trapped charges now cannot affect the plasma electrons because the electric field of the trapped charge is screened by the nuclei of the metal atoms.

Within this context, let us consider the emitted electric field intensity to have the simple form $E_o \sin(\omega t)$, where ω is the

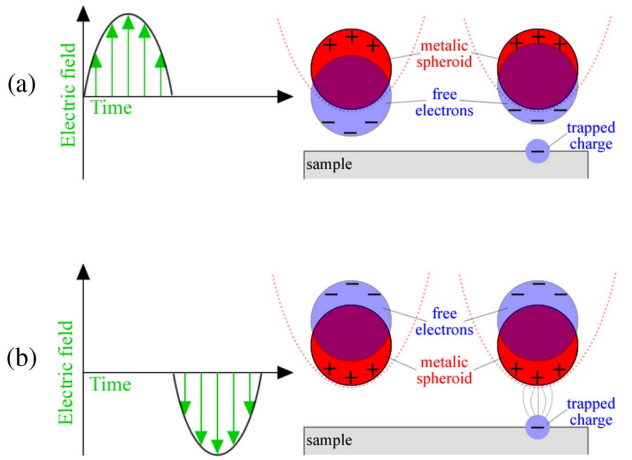

Fig. 1. Schematics of the localized surface plasmons excited by the oscillating electric field of an incident laser beam. The displacement of the plasma electrons (negative charge) relatively from the fixed lattice of atoms leaves a positive charge in the opposite direction; (a) in the first half-cycle of the oscillating electric field, the plasma electrons from the tip are affected by the presence of the charge trapped on the surface of the sample; (b) in the second half-cycle of the oscillating electric field, the trapped charge has no influence on the plasma electrons from the tip as the field is screened by the positive charge.

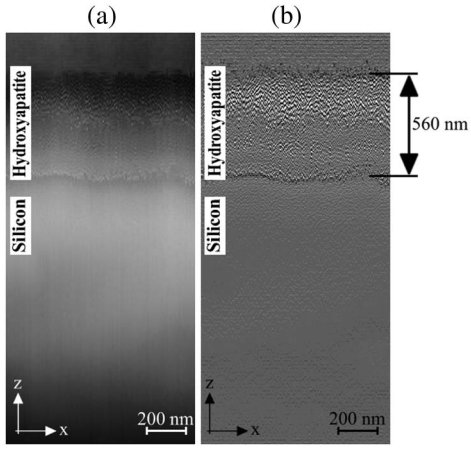

Fig. 2. AFM investigation in XZ plane to measure the thickness of the HA layer: (a) topography; (b) derivative of the topography image for better highlighting of the dimension of the HA layer.

angular frequency and t is time, and integrate it over a period T. In the absence of any trapped surface charge the light intensity will be proportional to the value $E_o^2/2$. Conversely, with trapped surface charges the emitted electric field intensity will be $(E_o - \Delta E) \cdot \sin(\omega t)$ in the first half-cycle and $E_o \sin(\omega t)$ in the second half-cycle. The intensity of the emitted light will then be proportional to a reduced factor, $E_o^2/4 + (E_o - \Delta E)^2/4$. This inherent variation in the light intensity due to the presence of trapped surface charge can be detected with nanoscale resolution in an s-SNOM.

We tested the above hypothesis in a practical setting on a hydroxyapatite (HA) thin film deposited on a silicon wafer by a spin-coating method. HA is one of the key biomaterials currently used for dental and orthopedic implants. Its dielectric properties and induced polarization have been investigated in recent years because of the influence of electron beam injected trapped charge in stimulating specific protein binding through Coulumbic interactions [12,13]. Details about the HA thin film fabrication procedure and about the ring-shaped negative charged areas can be found in previous publications [14–17]. Figure 2 shows atomic force microscopy (AFM) images in cross section. The thickness of the HA layer has been found to be approximately 560 nm. A 20 keV energy electron beam was used to irradiate the HA surface in a scanning electron microscope chamber at a pressure of 10^{-4} Pa. As a result, a trapping of charge at the location of surface defects takes place without any modification of the topography [14–17]. As it has been reported by these authors with the help of Kelvin probe force microscopy (KPFM), phase AFM, and photoluminescence (PL) measurements, the trapped charges injected from the electron beam lead to a negatively charged ring-shaped area on the surface.

In addition to the formation of a negative charged area on the HA surface, the electron beam can cause dissociation of residual hydrocarbons [17] that can lead to carbon contamination, as has been shown by AFM phase imaging [16].

The presence of the trapped charge caused PL, which was imaged with diffraction-limited submicrometer range resolution using a laser scanning microscopy technique [16]. Here we successfully demonstrate direct imaging of these trapped charges with one order of magnitude higher resolution using s-SNOM. As the resolution in s-SNOM depends on the dimensions of the scanning tip, much higher resolutions can be achieved with tips with a small radius of curvature.

s-SNOM investigations were conducted using a custom-made module working in a pseudoheterodyne detection scheme [18,19], which was implemented as an upgrade to a commercial Quesant Q-Scope 350 AFM. In such AFM-based configurations simultaneous s-SNOM and AFM imaging is possible, as the oscillatory movement of the cantilever tip, specific to the AFM tapping workmode, also enables higher harmonic demodulation for s-SNOM imaging. The light source used for the s-SNOM investigations was a semiconductor laser with a 638 nm wavelength and 0.1 mW power.

As a first step, simultaneous AFM and s-SNOM investigations have been performed. The AFM image [Fig. 3(a)] shows the absence of any topographic modification due to charge or carbon contamination. The AFM phase imaging [Fig. 3(b)], however, shows a disk shape corresponding to the carbon contamination [16]. The correspondence between the signals

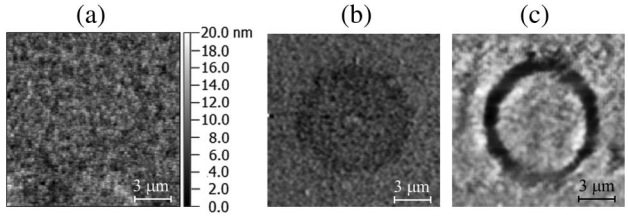

Fig. 3. AFM investigations on the HA sample: (a) topography of the sample, revealing a flat surface; (b) the same area investigated by AFM phase imaging, revealing a disk shape; (c) s-SNOM image (second harmonic demodulation) of the same area, revealing a ring-shaped structure.

recorded by AFM phase imaging and carbon contamination has been previously discussed in [16]. The s-SNOM image [Fig. 3(c)] reveals a ring-shaped structure which could be linked either to a change in the refractive index or to electric charge influence on the oscillating dipole, as hypothesized earlier.

For correctly assessing the influence of the trapped surface charge toward s-SNOM image formation, we have eliminated all possible influences that might lead to artifacts, which could bias the conclusions.

In the second step we ensured that PL, topographic features, and variations of the refractive index (due to the carbon contamination, for instance) did not introduce artifacts in the s-SNOM images that we had collected.

Regarding the PL, it is known that HA has a very large bandgap (3.95 eV) [20]. This means that it yields no PL for photon energy levels lower than the bandgap energy, which is the case of the visible range. However, in same cases, the PL, having less energy than the bandgap energy, was detected and could be attributed to localized energy levels (deep or shallow levels within the bandgap) [16,20]. These levels might even correspond to stoichiometry deviations in the crystalline lattice or might be radiation induced. Previously we reported a PL effect when the same samples were illuminateed by an Ar:ion laser beam (488 nm) [16]. No PL was detected when samples were excited with 633 nm (He–Ne) wavelength radiation.

To verify if topography artifacts influenced the content of the s-SNOM images in our case, special attention was given to the scanning parameters and to the roughness of the sample's surface. The scanning parameters were carefully chosen so that the AFM high-precision feedback system together with a low scanning speed ensured the absence of error signal artifacts [21]. Moreover, roughness analysis reported the absence of sample features with step-like topography edges. This ensures the absence of edge-darkening effects, another important topography-related artifact [21]. Indeed, the surface of the sample can be considered almost flat, which is confirmed by an average roughness (R_a) of 0.33 nm and a root mean square (RMS) of only 0.43 nm.

To investigate the influence of the refractive index in the s-SNOM image, the HA surface was investigated by using digital holographic microscopy (DHM); we have used a setup based on a Mach–Zehnder interferometer working in reflection mode [22,23]. The light source was a He–Ne laser of wavelength 633 nm, and a beam splitter was used for splitting the beam so as to produce the reference and the object waves. The holograms formed by the interference between the reference wave (a plane wave) and the object wave (reflected wave from the object) were captured with a CCD camera with 1024 × 1024 square pixels of 6.9 μm on a side. More details about the setup can be found in [24,25]. DHM is capable of measuring the phase changes of the reflected light coming from the interface between HA and the underlying silicon dioxide layer. The differences of light phase are related to different optical path lengths in the sample, and both geometric path and refractive index may influence the optical path. In our case the HA surface can be considered as flat as this has been shown by the AFM investigations. The surface of the silicon wafer is also flat and parallel to the HA surface. This ensured a constant geometric path along the surface of the sample. Thus, variations in light phase detected by DHM were generated only by variations of the refractive index. Note that the light phase images

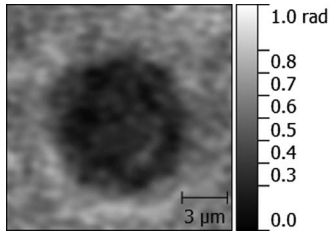

Fig. 4. Phase image of DHM investigation on the HA sample revealing a phase range between 0 and 1 rad.

measured by DHM are only related to the optical path lengths and are essentially different from phase images acquired by tapping mode AFM, which gives information about phase variations in the oscillation of the AFM cantilever. Figure 4 shows the DHM light phase image collected on a region where the charging procedure described earlier was applied.

Further, we have calculated the average DHM wave phase difference for a total number of 40 charged regions situated on the same HA sample, in order to determine the refractive index difference that occurs between the disk areas and the area which surrounds the disks. Using a custom MATLAB code, each individual disk region was enclosed in a square with an area double the area of the disk. Forty subimages were obtained this way, each containing a single disk and a background region of the same area. For each subimage, an image mask was created to differentiate the area exposed to the electron beam from the unexposed area. The image masks were created employing an edge detection algorithm based on the Canny method [26]. Using these masks, we have calculated the mean phase values for the disk areas and for the background areas. This procedure revealed a mean phase difference of 0.6 ± 0.2 rad between the areas exposed to the electron beam and the unexposed areas.

Taking into account that the HA layer has a thickness of 560 nm and that the refractive index of HA is about 1.65 [27] for the areas unexposed to the electron beam, the refractive index of the areas exposed to the electron beam has been derived to have a value of 1.6 ± 0.01. Thus, the index difference between the two regions is approximately 3%.

An important question to answer is, do such refractive index variations (3%) have a notable influence towards the recorded s-SNOM signals? For answering this question, we refer to our recent quantitative investigations regarding the dielectric function measurements with s-SNOM [28], which revealed a capability of measuring refractive index differences of more than 3.9% on SiO_2 and more than 5.7% on Si. Thus, a 3% index variation is indeed too small to be currently visualized by our s-SNOM system.

Summarizing, we demonstrated that the PL light does not influence the s-SNOM signal in our experiment. Furthermore, provided that the sample's surface is nearly flat and that it does not possess step-like topography edges, we conclude that the topography does not induce artifacts in the s-SNOM images. Moreover, the small change in refractive index (3%) revealed by DHM investigations and also the different shape (disk in DHM image, compared to ring shape in s-SNOM image) ensure a negligible influence of the refractive index variation on the s-SNOM images. The absence of all these factors entitles us to conclude that the s-SNOM image collected in the frame of our experiment depicts nothing else but the trapped charge that

was injected by electron beam bombardment on the HA surface.

Our experiment thus shows for the first time that s-SNOM can be employed for measuring trapped surface charge in dielectrics and semiconductors with subdiffraction resolution. This can be particularly useful in semiconductor devices where lithographic patterning through e-beam lithography and reactive ion etching may leave areas with trapped charges.

In conclusion, our experiments demonstrated that s-SNOM can be used to detect and map the surface trapped charge. This represents an important advantage of s-SNOM systems, especially for the cases when surface charge measurements with nanoresolution are needed. With more tools at hand for the assessment, characterization and tailoring of discrete electrostatic domains on biomaterials, such as HA, the scientific community will be able to expand the current understanding of the impact that surface charge holds over biological interactions between in-body elements and biomaterials. Such advancements are needed for developing novel surface charge patterning strategies that provide better integration of scaffolds and implants in the human body.

Funding. European Community's Seventh Framework Programme (FP7 BioElectricSurface 212533, FP7 LANIR 280804); Romanian Executive Agency for Higher Education, Research, Development and Innovation Funding (UEFISCDI) (PN-II-PT-PCCA-2011-3.2-1162 NANOLASCAN, PN-II-RU-TE-2014-4-1803 MICRONANO); Sectoral Operational Programme Human Resources Development (SOP HRD) funded by the European Social Fund and the Romanian Government (POSDRU/159/1.5/S/137390/).

Acknowledgment. G. A. S. and S. A. M. T. acknowledge the support of the European Commission. This communication reflects the views only of the authors, and the Commission cannot be held responsible for any use that may be made of the information contained therein. S. G. S. and R. H. acknowledge the support of UEFISCDI for part of their contribution. D. E. T. acknowledges the support of SOP HRD for part of his contribution. The authors acknowledge Dr. Maros Gregor and Professor Andrej Plecenick, Comenius University, Slovakia, for providing hydroxyapatite thin films with electron-beam injected trapped charges.

REFERENCES

1. A. A. Govyadinov, I. Amenabar, F. Huth, P. S. Carney, and R. Hillenbrand, J. Phys. Chem. Lett. **4**, 1526 (2013).
2. A. A. Govyadinov, S. Mastel, F. Golmar, A. Chuvilin, R. S. Carney, and R. Hillenbrand, ACS Nano **8**, 6911 (2014).
3. J. M. Stiegler, Y. Abate, A. Cvitkovic, Y. E. Romanyuk, A. J. Huber, S. R. Leone, and R. Hillenbrand, ACS Nano **5**, 6494 (2011).
4. J. M. Hoffmann, B. Hauer, and T. Taubner, Appl. Phys. Lett. **101**, 193105 (2012).
5. Z. Nuno, B. Hessler, B. Heiberg, R. Damato, T. Dunlap, Y. S. Shon, and Y. Abate, J. Nanopart. Res. **14**, 1 (2012).
6. M. Schnell, A. Garcia-Etxarri, A. J. Huber, K. Crozier, J. Aizpurua, and R. Hillenbrand, Nat. Photonics **3**, 287 (2009).
7. D. S. Kim and Z. H. Kim, Opt. Express **20**, 8689 (2012).
8. A. Horneber, K. Braun, J. Rogalski, P. Leiderer, A. J. Meixner, and D. Zhang, Phys. Chem. Chem. Phys. **17**, 21288 (2015).
9. T. W. Johnson, Z. J. Lapin, R. Beams, N. C. Lindquist, S. G. Rodrigo, L. Novotny, and S. H. Oh, ACS Nano **6**, 9168 (2012).
10. B. Knoll and F. Keilmann, Opt. Commun. **182**, 321 (2000).
11. A. Cvitkovic, N. Ocelic, and R. Hillenbrand, Opt. Express **15**, 8550 (2007).
12. S. Robin, A. A. Gandhi, M. Gregor, F. R. Laffir, T. Pecenik, A. Pecenik, T. Soulimane, and S. A. M. Tofail, Langmuir **27**, 14968 (2011).
13. T. Plecenik, S. Robin, M. Gregor, M. Truchly, S. Lang, A. Gandhi, M. Zahoran, F. Laffir, T. Soulimane, M. Vargova, G. Plesch, P. Kus, A. Plecenik, and S. A. M. Tofail, J. Mater. Sci. Mater. Med. **23**, 47 (2012).
14. T. Plecenik, S. A. M. Tofail, M. Gregor, M. Zahoran, M. Truchly, F. Laffir, T. Roch, P. Durina, M. Vargova, G. Plesch, P. Kus, and A. Plecenik, Appl. Phys. Lett. **98**, 113701 (2011).
15. R. Hristu, S. A. M. Tofail, S. G. Stanciu, D. E. Tranca, and G. A. Stanciu, *16th International Conference on Transparent Optical Networks (ICTON)* (2014).
16. R. Hristu, D. E. Tranca, S. G. Stanciu, M. Gregor, T. Plecenik, M. Truchly, T. Roch, S. A. M. Tofail, and G. A. Stanciu, Microsc. Microanal. **20**, 586 (2014).
17. R. Hristu, S. G. Stanciu, D. E. Tranca, and G. A. Stanciu, Appl. Surf. Sci. **346**, 342 (2015).
18. C. Stoichita, R. Hristu, S. G. Stanciu, and G. Stanciu, *3rd ICTON Mediterranean Winter Conference (ICTON-MW)* (2009).
19. N. Ocelic, A. Huber, and R. Hillenbrand, Appl. Phys. Lett. **89**, 101124 (2006).
20. G. Rosenman, D. Aronov, L. Oster, J. Haddad, G. Mezinskis, I. Pavlovska, M. Chaikina, and A. Karlov, J. Lumin. **122**, 936 (2007).
21. A. V. Zayats and D. Richards, *Nano-Optics and Near-Field Optical Microscopy* (Artech House, 2009).
22. A. Doblas, E. Sanchez-Ortiga, M. Martinez-Corral, G. Saavedra, P. Andres, and J. Garcia-Sucerquia, Proc. SPIE **8785**, 87856Q (2013).
23. A. Doblas, E. Sanchez-Ortiga, M. Martinez-Corral, G. Saavedra, and J. Garcia-Sucerquia, J. Biomed. Opt. **19**, 046022 (2014).
24. E. Sanchez-Ortiga, P. Ferraro, M. Martinez-Corral, G. Saavedra, and A. Doblas, J. Opt. Soc. Am. A **28**, 1410 (2011).
25. E. Sanchez-Ortiga, A. Doblas, G. Saavedra, M. Martinez-Corral, and J. Garcia-Sucerquia, Appl. Opt. **53**, 2058 (2014).
26. J. Canny, IEEE Trans. Pattern Anal. Mach. Intell. **6**, 679 (1986).
27. G. H. Bourne, *The Biochemistry and Physiology of Bone* (Elsevier, 2014).
28. D. E. Tranca, S. G. Stanciu, R. Hristu, C. Stoichita, S. A. M. Tofail, and G. A. Stanciu, Sci. Rep. **5**, 11876 (2015).